Nano Research

Open Access

Research Article

NIR photothermal enhancement to achieve high-efficiency nitrogen reduction to ammonia by polyoxometalates@Fe-polydopamine

Xiaofei Chen[1], Lixin Wu[2] ✉, and Feng Bai[1] ✉

[1] *Key Laboratory for Special Functional Materials of Ministry of Education, National & Local Joint Engineering Research Center for High-Efficiency Display and Lighting Technology, School of Nanoscience and Materials Engineering, Henan University, Kaifeng 475004, China*
[2] *State Key Laboratory of Supramolecular Structure and Materials, College of Chemistry, Jilin University, Changchun 130012, China*

Cite this article: *Nano Research*, **2025**, *18*, 94907006. https://doi.org/10.26599/NR.2025.94907006

ABSTRACT: The development of atmospheric pressure N_2 reduction to NH_3 is attracting much attention in green chemistry, yet it is still a challenge to obtain satisfactory activity under mild conditions. Herein, an efficient near-infrared (NIR) photothermal catalysis reduction of N_2 constitutes an occurrence is reported. With or without V-substitute polyoxometalates (POMs) loaded on the surface of Fe-chelated polydopamine (Fe-PDA) photothermal support through the electrostatic interactions, NIR photothermal catalysts POMs@Fe-PDA are fabricated. The induction of "FeV" cofactor facilitates electron transfer between V(V)/V(IV)&Fe(III)/Fe(II) and N_2, thereby activating N_2 molecule. The synergy between the catalytic activity of V-POMs and the local NIR photothermal effect of Fe-PDA dramatically enhances N_2 reduction. Noticeably, $PMo_{10}V_2$@Fe-PDA exhibits a significantly enhanced NH_3 production rate of 181.1 μmol·L^{-1} with a turnover frequency of 1006.1 mmol·M^{-1}·h^{-1} under 808 nm NIR laser radiation, being the highest values reported at atmospheric pressure. We expect that this work could provide an alternative approach for photothermal catalysis N_2 reduction under mild conditions.

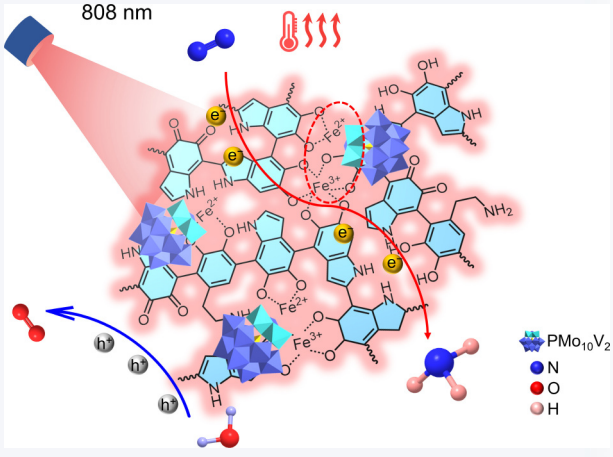

KEYWORDS: polyoxometalate, near-infrared photothermal catalysis, N_2 reduction, mild condition

1 Introduction

Ammonia (NH_3), as a potential carbon-neutral fuel and hydrogen carrier for vehicles, has garnered attention in green chemistry [1–4]. Considering strong nonpolar N≡N triple bond (941 kJ·mol^{-1}), the traditional synthesis of NH_3 faces unfavorable thermodynamics and sluggish kinetics characteristic, making necessary the use of high pressures and temperatures (i.e. 15–25 MPa and 673–873 K) to achieve adequate production rates [5]. Photo-driven fixation of N_2 to produce NH_3, taking H_2O as a proton source followed as the equation, $N_2 + 3H_2O \rightarrow 2NH_3 + 3/2O_2$, is considered to be one of the most ideal alternative ways, attributing to the mild conditions, low cost, and low energy consumption [6]. To date, various photocatalysts have been investigated for ammonia synthesis, such as metal oxide [7, 8], metal sulfide [9], and gold nanoparticles [10]. However, the solar-to-NH_3 efficiencies of most catalysts are still unsatisfactory due to two factors the low light utilization and rapid recombination of photogenerated electron–hole pair [11, 12]. Most of the catalysts can only absorb UV (< 400 nm) and visible light (400–700 nm), whereas the near-infrared (NIR) light (> 700 nm), accounting for 44% of the solar light cannot be effectively exploited. Although the photon energy of NIR light is not enough to meet the needs of most chemical reactions, the *in-situ* photothermal conversion capability has great potential for application in catalytic reactions. Therefore, developing sustainable photocatalytic N_2 fixation under milder conditions, especially in the NIR light regions, has become the most crucial issue facing us today.

Photothermal catalysis, as an emerging strategy to achieve chemical reactions, has attracted widespread attention in recent years due to its high reactivity obtained from the synergistic effect of thermocatalysis and photocatalysis [13, 14]. Recent research has shown that photothermal catalysts can expand the light absorption to the NIR region while ensuring efficient catalytic activity [15, 16], which offers a promising approach for N_2 reduction. Inspired by

Received: July 31, 2024; **Revised:** August 23, 2024
Accepted: August 25, 2024

✉Address correspondence to Feng Bai, baifengsun@126.com; Lixin Wu, wulx@jlu.edu.cn

the design of biological nitrogenase, the hetero-tetrametric MoFe and FeV proteins are considered to be the main catalytic centers [17]. The studies have shown that N_2 absorption and activation occurred at two reduced "belt" Fe(II) irons of FeMo cofactor with unoccupied d-orbits [18]. However, despite the structural similarity of the FeV cofactor and FeMo cofactor in nitrogenase, they exhibit different nitrogen reduction mechanisms, and it is not clear how metal compositions affect the catalytic performance and the possible mechanisms. To our knowledge, the FeV cofactors have not been reported in the field of photothermal catalytic nitrogen reduction.

Polydopamine (PDA) is one of the excellent photothermal materials due to most of the absorbed energy can be converted into heat in a nonradiative manner within 50 ps when there exists sufficient π–π packing [19, 20]. After Fe ions chelated with the catechol group in PDA, the strong ligand-to-metal charge transfer (LMCT) between electron donor–acceptor pairs can decrease the inherent energy band gap and promote the electron transfer, finally achieving the NIR light absorption enhancement of PDA [21, 22]. The generated Fe(II) is also an effective site for the adsorption and activation of N_2, the lack of V factor component severely hinders their application in photocatalysis. Polyoxometalates (POMs) are a type of anionic clusters constituted of transition metal oxides (V, W and Mo) connecting by sharing corners and edges [23–25]. Some low-valent transition metals endow the POMs with empty d-orbits. The multistep, rapid, and reversible electron transfer characteristics while maintaining structural integrity are considered to be the key core factors involved in redox reactions [26–28]. Especially, V-substituted POM has been proven to be an effective catalyst in photocatalytic N_2 reduction [29], but it is mainly concentrated in the ultraviolet–visible (UV–Vis) region, and the utilization of NIR light is still rarely reported. Based on the superiority of composition and structure, therefore, the design of a NIR photothermal catalyst with the coexistence of Fe and V-POM active sites is a potential strategy for photothermal catalytic N_2 reduction.

Herein, with or without V substituted POM, $H_5PMo_{10}V_2O_{40}$ ($PMo_{10}V_2$) and $H_3PMo_{12}O_{40}$ (PMo_{12}), are electrostatically attached to prepared Fe ions chelated PDA (Fe-PDA) nanoparticles, forming the NIR photothermal catalyst, $PMo_{10}V_2$@Fe-PDA and PMo_{12}@Fe-PDA (Scheme 1). After Fe ions are chelated, the photothermal effect of Fe(III)-PDA is enhanced. The Fe(II) generated in the process could adsorb and activate the N_2 well. Importantly, Fe-PDA, as a cation carrier, not only integrates the photothermal center and a uniformly distributed POMs catalytic center, but also maximizes the proximity of Fe and V catalytic sites. The experimental results show that V(IV) is the key intermediate of the reaction. The designed FeV cofactor materials not only adsorbed and activated N_2 molecules but also promoted electron transfer between generated V(V)/V(IV) and Fe(III)/Fe(II) and N_2, thus improving the charge separation efficiency. In collaboration with the NIR photothermal effect, achieving great improvement in catalytic activity for N_2 reduction. $PMo_{10}V_2$@Fe-PDA exhibits the NH_3 production of 181.1 μmol·L^{-1} NH_3 with the highest turnover frequency of 1006.1 mmol·M^{-1}·h^{-1}. This work provides an effective approach to achieve photothermal catalysis N_2 reduction under mild conditions.

2 Experimental

2.1 Materials and reagents

Dopamine hydrochloride (DA·HCl, 99%) and tris (2-amino-2-hydroxymethyl propane-1,3-diol) were purchased from Aladdin and used the next step without further purification. Ferric chloride hexahydrate ($FeCl_3·6H_2O$, 99%) was obtained from Beijing Chemical Industry Group Co., Ltd. $H_3PMo_{12}O_{40}$ was purchased from Sinopharm Chemical Reagent Co., Ltd. $H_5PMo_{10}V_2O_{40}$ was prepared according to the previously reported literature method [30]. Freshly distilled water (Millipore, 18.2 MΩ ·cm). $^{14}N_2$ (99.999%) and $^{15}N_2$ (99% ^{15}N, Wuhan Isotope Technology Co. Ltd) were purified before use (see Electronic Supplementary Material (ESM)).

2.2 Measurements

^1H NMR spectra are carried out on a Bruker Avance 500 MHz

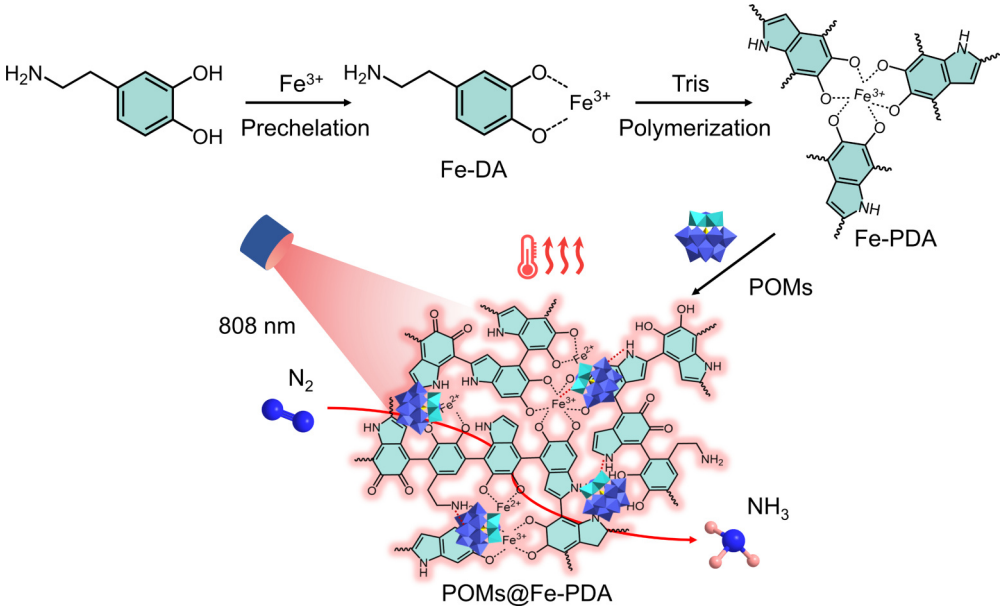

Scheme 1 Schematic drawing for the preparation of POMs@Fe-PDA and their photothermal catalysis processes in nitrogen fixation. (POMs represent $H_5PMo_{10}V_2O_{40}$ or $H_3PMo_{12}O_{40}$ cluster, while only $H_5PMo_{10}V_2O_{40}$ is shown here).

spectrometer (Germany) by using tetramethylsilane (TMS) as an internal reference. Fourier transform infrared spectroscopy (FT-IR) spectra (KBr pellet) are collected on a Bruker Vertex 80 V spectrometer (Germany) equipped with a DTGS detector (32 scans) with a resolution of 4 cm^{-1}. UV–Vis–NIR absorption spectra are obtained on a Lambda 365 spectrometer (PE). Dynamic light scattering (DLS) and Zeta potential measurements are made on the Zetasizer NanoZS instrument (Malvern Instruments). X-ray photoelectron spectra (XPS) and valence band spectra are measured on the ESCALAB-250 spectrometer using a monochromatic X-ray source (Al Kα line, 1486.6 eV), and the peak was corrected using the C1s binding energy position of 284.6 eV. Transmission electron microscopy (TEM) images are obtained on a field emission transmission electron microscope (JEOL JEM-2100F, Japan) with an accelerating voltage of 200 KV without staining. Scanning electron microscopy (SEM) images are performed on a JEOL JSM-6700F (Japan) field emission scanning electron microscope. *In situ* diffuse reflectance infrared Fourier-transform (DRIFT) spectroscopy was collected on the Thermo Fisher IN10. Near-infrared photothermal conversion experiment uses an 808 nm laser light source with adjustable output power (Xi'an Hongxiang Laser Technology Co., Ltd.). Electron paramagnetic resonance (EPR) was used on a JESFA200 instrument (Japan).

2.3 Preparation of POMs@Fe-PDA nanoparticles

Fe-PDA. According to the modified method in Ref. [21], a mixture of DA·HCl (100 mg, 0.58 mmol) and $FeCl_3{\cdot}6H_2O$ (15.68 mg, 0.058 mmol) was dissolved in deionized water (150 mL) with a molar ratio of 10:1. The solution was stirred vigorously for 1 h at room temperature. Then, 50 mL tris(hydroxymethyl)aminomethane (Tris) aqueous solution (70.26 mg, 0.58 mmol) was quickly added to the above solution to start polymerization. After 12 h, the expected Fe-PDA nanoparticles (NPs) were collected by centrifugation at 10,000 rpm for 15 min and washed three times with deionized water and ethanol for the next step.

POMs@Fe-PDA. To a 250 mL round-bottomed flask was added 100 mg Fe-PDA and 100 mL of deionized water, and the suspension was sonicated for 30 min to form a uniformly dispersed solution. 80 mg of $H_3PMo_{12}O_{40}$ or $H_5PMo_{10}V_2O_{40}$ aqueous solution was added dropwise with stirring quickly. After 12 h, simple centrifugation and washing with water to remove the excess of $H_3PMo_{12}O_{40}$ or $H_5PMo_{10}V_2O_{40}$ obtained the composite.

2.4 NIR photothermal conversion properties

The photothermal conversion performance of POMs@Fe-PDA was evaluated by monitoring the temperature variety. Specifically, 0.5 $mg{\cdot}mL^{-1}$ $PMo_{10}V_2$@Fe-PDA aqueous solution was put in a quartz cuvette, irradiated by the NIR laser light (808 nm, 1 $W{\cdot}cm^{-2}$). The temperature of the solution gradually increased until it remained stable and was recorded every 30 s with an IR thermal imaging camera. After the temperature remains constant, turn off the laser and record the changes in the cooling period. The temperature change of the deionized water was monitored as the control panel under the identical operation.

2.5 NIR photothermal catalytic activity measurement

In general, 3 mg of $PMo_{10}V_2$@Fe-PDA was dispersed in 3 mL of water by ultrasound and then sealed in a 5 mL round-bottom quartz bottle. Before illumination, the treated high-purity N_2 (100 $mL{\cdot}min^{-1}$) was continuously bubbled into the flask for 10 min to make sure the whole system was completely under the N_2 atmosphere. The whole system was kept in dark and closed conditions. Then the NIR laser (808 nm, 1 $W{\cdot}cm^{-2}$) radiation was performed for photothermal catalytic reaction. Once the reaction finished, the catalyst was separated by filtration, 1.0 mL of the reaction solution was taken and 4 mL H_2SO_4 solution (0.5 mM) was added. The concentration of produced NH_3 was monitored by the indophenol blue method. The catalyst was washed with water and ethanol and reused for the next catalytic cycle after drying in a vacuum oven at 50 °C for 24 h. As a control, the reaction was carried out at room temperature and external heating in an oil bath under dark conditions. To avoid the influence of trace amounts of NH_3 in the air and in most water exposed to air, herein, fresh ultrapure water was used in the N_2 fixation experiments. All the measured values of ammonia content are the average results of three experiments.

2.6 ^{15}N isotopic labeling experiment

The isotope labeling experiment used $^{15}N_2$ as the feed gas, and the ^{15}N enrichment was 99% (Wuhan Isotope Technology Co., Ltd.). Firstly, the oxygen and air in the round bottom flask and solvent H_2O were fully removed by three freeze–vacuum–thaw cycles. Then, feed gas $^{15}N_2$ was bubbled for 10 min with a flow rate of 30 $mL{\cdot}min^{-1}$. Following the same method, ensuring that there is only $^{15}N_2$ in the final reaction vessel. After that, insert a balloon filled with $^{15}N_2$ into the reaction vessel to ensure the source of $^{15}N_2$ in subsequent reactions. Note that considering the possible contamination caused by $^{14}N_2$ in the air, the entire system is kept closed. After photothermal catalytic $^{15}N_2$ reduction for 6 h, the catalyst was filtrated, the obtained solution was concentrated, and the pH of the solution was adjusted to 2–3 with 0.1 M HCl. Then add 0.1 mL of the above solution to 0.5 mL DMSO-d_6. The produced $^{15}NH_4^+$ was identified using ^1H NMR spectroscopy.

3 Results and discussion

3.1 Preparation and characterization of POMs@Fe-PDA

The synthetic route of uniformly dispersing POM clusters on the Fe-PDA supports is illustrated in Scheme 1. The synthesis and characterization of Fe-PDA precursors are summarized in the Supporting Information (Figs. S1 and S2 in the ESM). After adding the aqueous solution with an excess of $PMo_{10}V_2$ or PMo_{12} dropwise to the Fe-PDA suspension with pre-acidification with HCl (1 $mol{\cdot}L^{-1}$), the ionic complexes of Fe-PDA and POMs, $PMo_{10}V_2$@Fe-PDA and PMo_{12}@Fe-PDA were collected. After the filtration and washing with water, the counterions of both POMs and Fe-PDA, as well as nonbonded POMs, are excluded. FT-IR spectra show that the characteristic vibration bands of $PMo_{10}V_2$ in $PMo_{10}V_2$@Fe-PDA located at 1049, 949, 860 and 790 cm^{-1} correspond with the stretching vibration modes of P–O, Mo=O and Mo–O–Mo (Fig. S3 in the ESM). The slight shifting with respect to the bare $PMo_{10}V_2$ can be well attributed to the effect of electrostatic interaction [27]. Since POMs have abundant surface oxygens, the surrounding discrete anions can electrostatically bind with Fe-PDA. The bands of PMo_{12} in PMo_{12}@Fe-PDA also have a slight with the vibration bands of bare PMo_{12}, demonstrating the cluster structure stability and its binding with Fe-PDA (Fig. S3 in the ESM). The Fe-PDA can assemble with POMs through electrostatic interaction, which could be further demonstrated by

the more negative zeta potential of $PMo_{10}V_2$@Fe-PDA (−34.1 mV) and PMo_{12}@Fe-PDA (−30.5 mV) than that of Fe-PDA (−26.1 mV) (Fig. S4 in the ESM). The inductively coupled plasma (ICP) results and organic elemental analysis (Table S1 in the ESM) give the mass contents of $PMo_{10}V_2$ and PMo_{12} in the final POMs@Fe-PDA reaching up to 64.26% and 65.29% (based on P).

In line with the XPS of Fe-PDA, the $PMo_{10}V_2$@Fe-PDA spectrum not only presented the peak of C 1s, N 1s, O 1s and Fe 2p, but the peaks of P 2p, V 2p and Mo 3d also be observed (Fig. S5(a) in the ESM). As for the Fe 2p spectrum, the ratio of Fe(III) to Fe(II) (84.4%:15.6%) is consistent with Fe-PDA (Fig. S5(b) in the ESM), which was not affected by $PMo_{10}V_2$. The characteristic N 1s peak only contains three forms: binding energy at 399.1 eV belonged to pyrrolic N, the main form of the N element in $PMo_{10}V_2$@Fe-PDA (Fig. S5(c) in the ESM); the binding energy at 402.1 and 398.6 eV corresponds to N–C and –N=C of Fe-PDA. The above analysis proves that the surface of the prepared catalyst does not contain other forms of Fe, C and N, avoiding the influence of impurities on N_2 reduction. And the valence states of metal element V remain at their highest valence which is identical to the bare $PMo_{10}V_2$ (Fig. S5(d) in the ESM). Also, the elements Fe and N in PMo_{12}@Fe-PDA were also clearly identified and the elements Mo kept the highest valent (Fig. S6 in the ESM). Furthermore, the SEM and TEM images show the $PMo_{10}V_2$@Fe-PDA nanoparticles are spherical in shape with a uniform particle size distribution of 140–160 nm in diameter (Figs. 1(a) and 1(b)). The TEM result is basically consistent with the hydrated particle sizes (about 164 nm) (Fig. 1(b), insert), proving the good dispersibility of $PMo_{10}V_2$@Fe-PDA in water. The high-resolution transmission electron microscopic (HRTEM) image shows a homogeneous distribution of $PMo_{10}V_2$ (~ 1 nm) in dark spots on the Fe-PDA spherical nanoparticles (Fig. 1(c) and insert). This shows that PDA is a good carrier and can effectively avoid POMs aggregation. Similarly, the SEM and TEM results of PMo_{12}@Fe-PDA display the spherical nanoparticles and the even distribution of PMo_{12} can be clearly seen in the enlarged picture (Figs. 1(d)–1(f)). Furthermore, the uniform element distribution (Figs. 1(g) and 1(h)) and energy-dispersive X-ray spectroscopy (EDX) energy spectra (Fig. S7 in the ESM) support POMs that are uniformly distributed on the self-assembled structures. These results definitely point out that the POMs@Fe-PDA are universal and their assembly structures are less relevant to the molecular composition of POMs.

3.2 NIR photothermal property of POMs@Fe-PDA

During photothermal catalysis, the efficient transformation of NIR light into heat is an important evaluation indicator. From the UV–Vis–NIR spectra (Fig. 2(a)), Fe-PDA dispersions exhibit a broad optical absorption and have more intense absorption in the

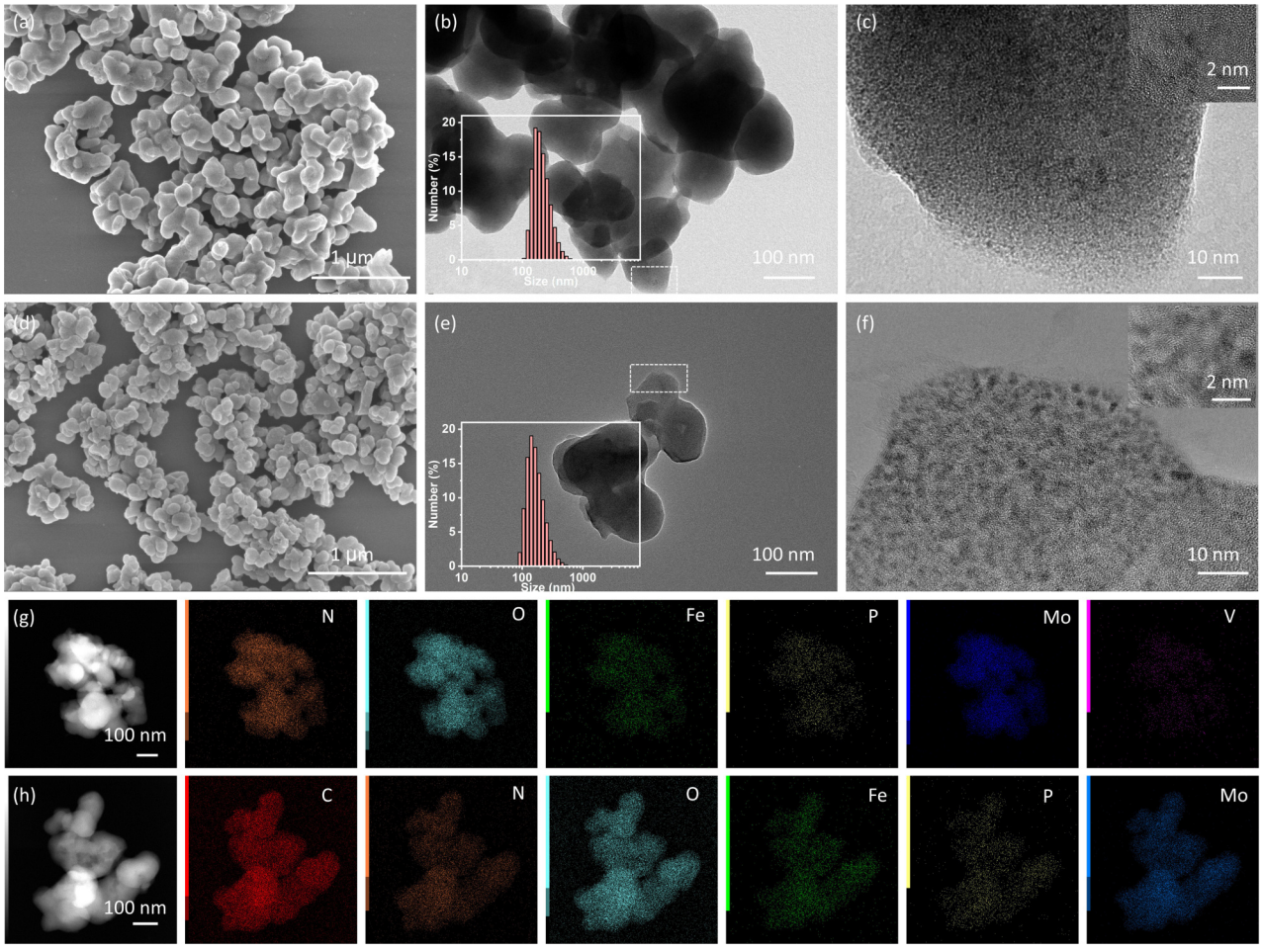

Figure 1 (a) SEM and (b) TEM images of $PMo_{10}V_2$@Fe-PDA and (c) HRTEM image taken from (b), where the insert is a local amplification of the spots. (d) SEM and (e) TEM images of PMo_{12}@Fe-PDA and (f) HRTEM image taken from (e), where the insert is a local amplification of the spots. The inserts in (b) and (e) are the hydration particle size and distribution of $PMo_{10}V_2$@Fe-PDA and PMo_{12}@Fe-PDA, respectively. EDS mapping images of (g) $PMo_{10}V_2$@Fe-PDA and (h) PMo_{12}@Fe-PDA.

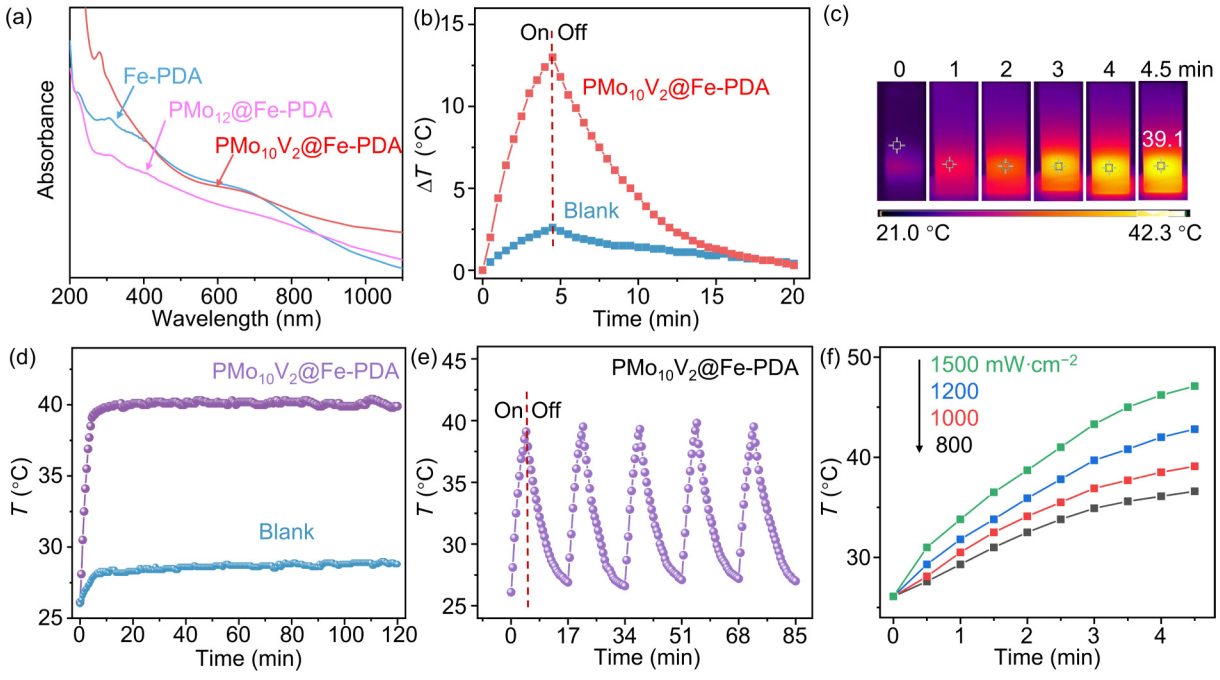

Figure 2 (a) UV–Vis–NIR absorption spectra of Fe-PDA, PMo_{12}@Fe-PDA, and $PMo_{10}V_2$@Fe-PDA complex dispersions. (b) The temperature change plots of pure water and $PMo_{10}V_2$@Fe-PDA dispersion under the NIR laser radiation (808 nm, 1.0 W·cm^{-2}). (c) IR thermal images of $PMo_{10}V_2$@Fe-PDA solution under NIR light radiation. (d) The temperature variation curve of $PMo_{10}V_2$@Fe-PDA solution and pure water under the continuous radiation of the NIR laser. (e) The temperature variable curves of $PMo_{10}V_2$@Fe-PDA dispersion upon turning on and off the NIR laser in five cycles. (f) The time-dependent temperature of the $PMo_{10}V_2$@Fe-PDA dispersions under different NIR laser intensities.

visible to near-infrared bands. This may be because Fe(III) can serve as an electron acceptor with strong electron-withdrawing properties and coordinate with catechol groups to form many donor–acceptor pairs in Fe-PDA. Considering that dopamine is a ligand and the high oxidation state Fe(III) is present in the Fe-PDA nanoparticle system, the LMCT is the only possible transition: i.e., phenolic oxygen to empty Fe(III) charge transfer between orbitals, thereby achieving the characteristics of high band intensity and wider spectral bands [21]. It can be seen that the introduction of POMs does not affect the absorption of Fe-PDA in the near-infrared region, and the prepared PMo_{12}@Fe-PDA and $PMo_{10}V_2$@Fe-PDA still maintain the absorption in the NIR region well.

Then the photothermal conversion efficiency of the $PMo_{10}V_2$@Fe-PDA dispersions under NIR laser (808 nm, 1 W·cm^{-2}) is evaluated. By monitoring the thermal profile change with time under the on–off operation of the NIR laser, the temperature difference (ΔT) could rise about 13 °C within 4.5 min (Fig. 2(b)), while the pure water only increases to 2.6 °C. The maximum temperature of $PMo_{10}V_2$@Fe-PDA can reach 39.1 °C (Fig. 2(c)) and maintain 39.7 ± 0.6 °C for at least 2 h (Fig. 2(d)). The η is calculated to be 37.43%, which is comparable to the PDA materials in published results [31–33]. The detailed derivation process is presented in the ESM and Fig. S8 in the ESM. No obvious thermal loss is observed in five cycles (Fig. 2(e)), indicating sustainable photothermal stability. Furthermore, the $PMo_{10}V_2$@Fe-PDA also shows light intensity dependence (Fig. 2(f)), and the temperature of dispersions will increase accordingly as the optical power density increases. Similarly, the NIR photothermal conversion efficiency of PMo_{12}@Fe-PDA dispersion is characterized with the same method, the η is 35.67% (Figs. S9(a)–S9(c) in the ESM). The PMo_{12}@Fe-PDA also still maintains the photothermal conversion performance in five cycles (Fig. S9(d) in the ESM) and 38.4 ± 0.5 °C for at least 2 h (Fig. S9(e) in the ESM). Considering that photothermal catalytic reactions are performed under thermal conditions, the stability of the catalyst under heating conditions is very critical. To further confirm it, the hydrodynamic size changes of $PMo_{10}V_2$@Fe-PDA were evaluated in the range of 20–60 °C, and the particle size was almost maintained at 140–180 nm, indicating the stability of the prepared composite under heating conditions (Fig. S10 in the ESM).

3.3 Photothermal catalysis performance of POMs@Fe-PDA

Since the POMs@Fe-PDA exhibit good NIR photothermal conversion ability, the photothermal catalysis performance of N_2 reduction is evaluated under the NIR laser radiation (808 nm, 1 W·cm^{-2}). According to a rigorous experimental protocol, a series of tests were performed to obtain reliable evidence of N_2 reduction activity [34, 35]. As shown in Figs. S11 and S12 in the ESM, no NH_3 contaminants are observed in the fully purified gas ($^{14}N_2$ and $^{15}N_2$). The concentration of NH_3 was measured by the indophenol blue method (Figs. S13 and S14 in the ESM). All the photothermal catalytic reactions of N_2 reduction are carried out with pure water as the proton source and solvent without any other electronic sacrificial agents and cocatalysts, which decreases the complexity and cost of the reaction. The results are summarized in Table 1. As a control, the catalytic experiments are performed under similar conditions except that the temperature is replaced with the external heating or room temperature in the dark environment. The blank panels show that N_2 reduction can hardly occur in the absence of catalysts (Table 1, entries 1–3). In contrast, the excellent catalytic activity of N_2 fixation is observed in the presence of $PMo_{10}V_2$@Fe-PDA under NIR laser light radiation (Table 1, entry 4). It is seen that the NH_3 production is as high as

Table 1 The summary for NH_3 production upon series catalysts in water at different conditions[a]

Entry	Catalyst	Condition[b]	NH_3 production (μmol·L^{-1})[c]	TOF (mmol·M^{-1}·h^{-1})[d]
1	Blank	NIR (40 °C)	0.9	—
2		Dark (40 °C)	1.4	—
3		Dark (R.T.)	0.8	—
4	$PMo_{10}V_2$@Fe-PDA	NIR (40 °C)	181.1	1006.1
5		Dark (40 °C)	8.2	40.0
6		Dark (R.T.)	2.3	12.8
7		Dark (90 °C)	29.1	161.7
8	Fe-PDA	NIR (40 °C)	19.1	—
9		Dark (40 °C)	2.5	—
10		Dark (R.T.)	1.2	—
11	$PMo_{10}V_2$	NIR light	3.9	—
12		Dark (40 °C)	4.0	—
13		Dark (R.T.)	2.5	—
14	$PMo_{10}V_2$/Fe-PDA	NIR (40 °C)	98.6	547.8
15		Dark (40 °C)	7.2	40
16		Dark (R.T.)	1.9	10.6
17	PMo_{12}@Fe-PDA	NIR (40 °C)	123.1	647.9
18		Dark (40 °C)	7.6	40.0
19		Dark (R.T.)	2.0	10.5

[a] Reaction conditions: catalysts (3.0 mg, 0.18 μmol·mL^{-1} based on Fe and $PMo_{10}V_2$), N_2 (100 mL·min^{-1}), 60 min. [b] NIR laser (808 nm, 1.0 W·cm^{-2}). [c] It is measured via the indophenol blue method. [d] TOF: (NH_3 production)/(moles of Fe and POMs) × time.

181.1 μmol·L^{-1} after only 60 min. Notably, the TOF value is up to 1006.1 mmol·M^{-1}·h^{-1}, which is the highest NH_3 generation result in POM-based and Fe/V doping catalysts (Table S2 in the ESM). When changing to external heating, the production decreases rapidly and becomes weak at 40 °C and even lower at room temperature (Table 1, entries 5 and 6). When the temperature is 90 °C with external heating under dark conditions (Table 1, entry 7), the production rate of NH_3 increases slightly, but it is much lower than the catalytic activity under NIR photothermal conditions, reflecting the advantages of *in-situ* photothermal catalysis of NIR light. The conversion enhancement factor of photothermal-to-thermal catalysis at different times is shown in Fig. S15(a) in the ESM. The introduction of the photothermal effect showed a 70–80 fold total enhancement, with a 19–23 fold local enhancement coming from the high local temperature in the vicinity of the nano-heater core Fe-PDA. The production rate of NH_3 is almost linearly dependent on the light intensity (Fig. S15(b) in the ESM). Definitely, the reaction rate under NIR radiation is much higher than the reaction rate at the same measured temperature with external heating. In principle, external heating reaches the catalytic center through the continuous collision of solvent molecules and thermal diffusion. In contrast, under the NIR light radiation, the Fe-PDA carrier directly transfers the heat source generated by photothermal conversion to N_2 molecules adsorbed on the POM through remote radiation control, that is *in-situ* heating. Therefore, the near-infrared photothermal effect is more conducive to accelerating the N_2 reduction reaction.

To make a further comparison, the individual components in the composite catalysts are evaluated under the same conditions at room and reaction temperatures by external heating and NIR photothermal transformation. Fe-PDA component shows a certain enhanced catalytic activity under photothermal conditions due to the strong photo-response of Fe-PDA to NIR light and the empty d orbital of Fe(II) can be used as the adsorption site for N_2 (Table 1, entry 8). The negligible efficiency is observed under external heating and room temperature conditions (Table 1, entries 9 and 10). $PMo_{10}V_2$ component also exhibits very weak NH_3 production efficiency under the test conditions (Table 1, entries 11–13). When the two components were simply mixed as a catalyst, the efficiency of NH_3 generation increased significantly to 98.6 μmol·L^{-1} under NIR light conditions, but this was still lower than that of the prepared catalyst. It is speculated that the decrease in yield is caused by the agglomeration of POM during the reaction, indicating the necessity of electrostatic interaction between Fe-PDA carriers and $PMo_{10}V_2$. Similarly, it does not work in external heating and ambient temperature conditions (Table 1, entries 14–16).

To demonstrate the universality of the present strategy, the catalytic performance of PMo_{12}@Fe-PDA with or without NIR laser radiation is accessed (Table 1, entries 17–19). The reduction rate of N_2 also reached 123.1 μmol·L^{-1} in 60 min with a TOF value of 647.9 mmol·M^{-1}·h^{-1} under NIR laser light, in comparison to only 7.6 μmol·L^{-1} (40 mmol·M^{-1}·h^{-1}) and 2.0 μmol·L^{-1} (10.5 mmol·M^{-1}·h^{-1}) under the external hating and ambient temperature, respectively, indicative of NIR photothermal enhancement. Compared with the reported results for N_2 fixation catalyzed by POMs-based photocatalysts, it can be found that the POMs@Fe-PDA also have a better catalytic performance, supporting the advantages of NIR photothermal conversion.

To further investigate the reaction process, the NH_3 production curves catalyzed by Fe-PDA, POMs and POMs@Fe-PDA are examined at different time intervals (Figs. 3(a) and 3(b)). Compared to Fe-PDA and POMs, the production rate in the presence of POMs@Fe-PDA exhibits an upward trend with increasing reaction time, suggesting that both the combination of

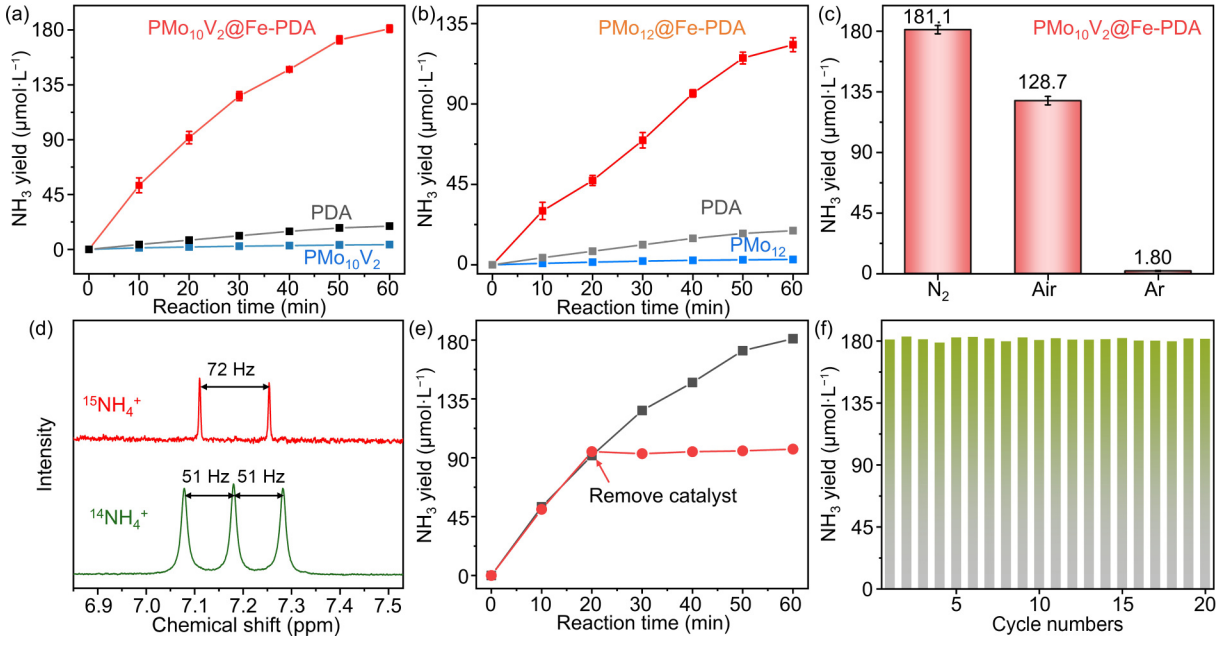

Figure 3 NH_3 production curves versus the time of N_2 reduction catalyzed (a) by Fe-PDA, $PMo_{10}V_2$ and $PMo_{10}V_2$@Fe-PDA and (b) by Fe-PDA, PMo_{12} and $PMo_{10}V_2$@Fe-PDA under the NIR laser radiation. (c) NH_3 production in different gas environments catalyzed by $PMo_{10}V_2$@Fe-PDA. (d) ^1H NMR spectra of produced NH_4^+ over $PMo_{10}V_2$@Fe-PDA using the purified $^{14}N_2$ and $^{15}N_2$ gas, respectively. (e) Leaching test on the NH_3 production in the N_2 fixation with or without $PMo_{10}V_2$@Fe-PDA. (f) Recycling test data in 20 runs.

POMs with Fe-PDA and the NIR photothermal conversion promote the catalysis. When the reaction is carried out in an air atmosphere, the generation rate of NH_3 decreases to 90.5 μmol·L^{-1} (for PMo_{12}@Fe-PDA) and 128.66 μmol·L^{-1} (for $PMo_{10}V_2$@Fe-PDA) (Fig. 3(c) and Fig. S15(c) in the ESM). The formation of NH_3 is not detected in argon as a control, indicating the formation of NH_3 is derived from the infused N_2. To further confirm the source of NH_3 generated from photothermal catalysis N_2 reduction, isotope labeling experiments using $^{15}N_2$ as the nitrogen source are performed. The ^1H NMR spectrum of the NH_3 by catalyzing $PMo_{10}V_2$@Fe-PDA under $^{14}N_2$ atmosphere shows triplet peaks with the coupling constant 51 Hz that represent $^{14}NH_4^+$ (Fig. 3(d)), when using $^{15}N_2$ as the feeding gas, only doublet peaks with a coupling constant of 72 Hz matching well with the $^{15}NH_4^+$ standard can be detected, providing strong proof that the produced NH_3 is directly formed from the dissociative nitrogen molecules at ambient conditions through the constructed $PMo_{10}V_2$@Fe-PDA rather than the catalyst itself [36]. Considering that the used $PMo_{10}V_2$@Fe-PDA has an additional N source stemming from the PDA in $PMo_{10}V_2$@Fe-PDA, high-purity N_2 sources ($^{15}N_2$) may face contamination in photothermal catalytic N_2 reduction experiments. To exclude the possibility, elemental analysis results show the N (wt.%) is only 3.64% for $PMo_{10}V_2$@Fe-PDA and 4.15% for PMo_{12}@Fe-PDA. The N content is very low in the limited catalyst dosage. Therefore, even if the N in the catalyst is present in the form of ^{14}N, this has a negligible effect on the reduction of $^{15}N_2$ to ammonia.

3.4 Stability of catalysts in recycling use

To reveal the stability of the catalyst, the leaching experiment over POMs@Fe-PDA was carried out. They are filtered out during the reaction, and the detected NH_3 generation no longer increases (Fig. 3(e) and Fig. S15(d) in the ESM), and the yield did not increase even when the temperature reached 90 °C with the external heating, indicating that the prepared catalyst did not leak into the solution. This can also further prove that there are no impurity ions or interferants in the reaction solution that interfere with the indophenol blue method employed to quantify NH_3 yield. Moreover, the ICP results also showed that no metal ions were detected in the filtrate (Table S3 in the ESM). The $PMo_{10}V_2$@Fe-PDA and PMo_{12}@Fe-PDA also demonstrate good photothermal catalysis stability, since no obvious decrease in the performance is observed in 20 repetitive cycles, showing great potential for long-term artificial ammonia synthesis (Fig. 3(f) and Fig. S15(e) in the ESM). After filtration, it was washed with water and ethanol, and then dried in a vacuum oven for the next use.

The FT-IR spectrum of the recovered $PMo_{10}V_2$@Fe-PDA and PMo_{12}@Fe-PDA (Fig. S16 in the ESM) is the same as the initial state, revealing the well-maintained composition. In the photocatalytic N_2 reduction, many groups further highlight the importance of catalyst cleanliness. Some adventitious impurities on the surface of the photocatalyst can act as an active species to promote reactions that were not originally possible on the catalyst surface, bringing complexity to the analysis of synthesized NH_3 [37, 38]. Then, it is necessary to make sure of the local coordination environment of the Fe sites and N species. Compared with the initial catalyst, the valence states of Fe and POM in the recovered catalyst did not change, and the ratio of Fe(III) to Fe(II) is basically maintained at 83.3%:16.7% (Figs. S17 and S18 in the ESM). The N 1s spectrum shows that there are still three forms and pyrrole N is the main form, which indicates that there has been little change in the chemical environment of N. The organic and elemental analysis of the used catalysts after 20 recycles is consistent with the fresh one, suggesting the used catalysts have little dissociation or decomposition (Tables S4 and S5 in the ESM).

3.5 Possible mechanism of N_2 fixation

To explore the catalysis process of $PMo_{10}V_2$@Fe-PDA, the possible

mechanism is studied. It is necessary to clarify the electronic band structure of each component in the composite catalysts. The UV–Vis diffuse reflectance spectra (DRS) (Fig. S19 in the ESM) show the band gap energies (E_g) of PDA, PMo_{12} and $PMo_{10}V_2$, PMo_{12}@Fe-PDA and $PMo_{10}V_2$@Fe-PDA can be obtained at 1.83, 2.41, 2.11, 1.68, 1.73 eV, respectively. The ultraviolet photoemission spectroscopy (UPS) is utilized to calculate the highest occupied molecular orbital (HOMO) energy and valence band energy of the materials. As shown in Figs. S20–S23 in the ESM, the cutoff energy (E_{cutoff}) and Fermi energy (E_{Fermi}) are derived from the low binding energy and high binding energy regions through the corresponding tangent lines, respectively. The $E_{VB/HOMO}$ of PDA, PMo_{12}, $PMo_{10}V_2$, PMo_{12}@Fe-PDA and $PMo_{10}V_2$@Fe-PDA is 0.75, 2.21, 1.58, 1.15, 1.04 V versus NHE, respectively (the detailed calculation process is listed in Fig. S20 in the ESM). The $E_{CB/LUMO}$ could be obtained by the difference of VB/HOMO energy level and E_g. Based on these results, the electronic structure distributions are illustrated in Fig. 4(a). After loading Fe-PDA, the CB energies of PMo_{12}@Fe-PDA and $PMo_{10}V_2$@Fe-PDA become more negative than the bare POMs and lower than the reductive potential of N_2/NH_3 (−0.05V), which makes N_2 reduction thermodynamically feasible. Meanwhile, the VB energies are higher than the oxidation potential of H_2O, indicating the H_2O will oxidize to O_2 by the photogenerated holes ($2H_2O + 4h^+ \rightarrow O_2 + 4H^+$), thus reducing the carrier recombination in catalysis. Then, a possible mechanism is proposed. Under NIR laser excitation, the photothermal effect of Fe-PDA promotes the formation of energetic electrons (Fig. 4(b)) [39]. The photoexcited electrons of Fe-PDA can be transferred by $PMo_{10}V_2$, and then delivered to the absorbed N_2, followed by a succession of reduction of $PMo_{10}V_2$. The more negative CB energy indicates that the photogenerated electrons of PDA are more easily transmitted to $PMo_{10}V_2$, leading to a good performance of N_2 reduction.

To further clarify the role of Fe and V in the N_2 reduction process, considering the NH_3 produced by photothermal catalysis of $PMo_{10}V_2$@Fe-PDA is 1.47 times that of PMo_{12}@Fe-PDA, and we speculated that this may be due to the presence of V. Because V has a stronger redox ability than Mo, when V is introduced into POMs instead of Mo, the primary structure and reactivity of POMs could be changed. Based on this, the catalyst $PMo_{10}V_2$@Fe-PDA is first characterized by the EPR spectra. The results show two distinct signals appear at 1628 and 3534 G, which are caused by the Fe^{3+} and PDA, respectively (Fig. 4(c), black) [17]. Since the V and Mo in $PMo_{10}V_2$@Fe-PDA are in their highest valence state, they are signals silent. Then, *in-situ* EPR spectra are tested again over $PMo_{10}V_2$@Fe-PDA during the NIR laser light radiation under an N_2 atmosphere. The signal peak of the reduced V(IV) was detected and the signal intensity of Fe^{3+} obviously enhanced (Fig. 4(c), red), suggesting the conversion from Fe^{2+} to Fe^{3+} after N_2 adsorption [40]. Then, *in situ* DRIFT spectroscopy was performed to monitor the possible intermediate products. *In situ* DRIFT spectra show that the signal of N-containing intermediates is gradually boosted with time under illumination (Fig. 4(d)). The absorption bands at 3569 cm^{-1},

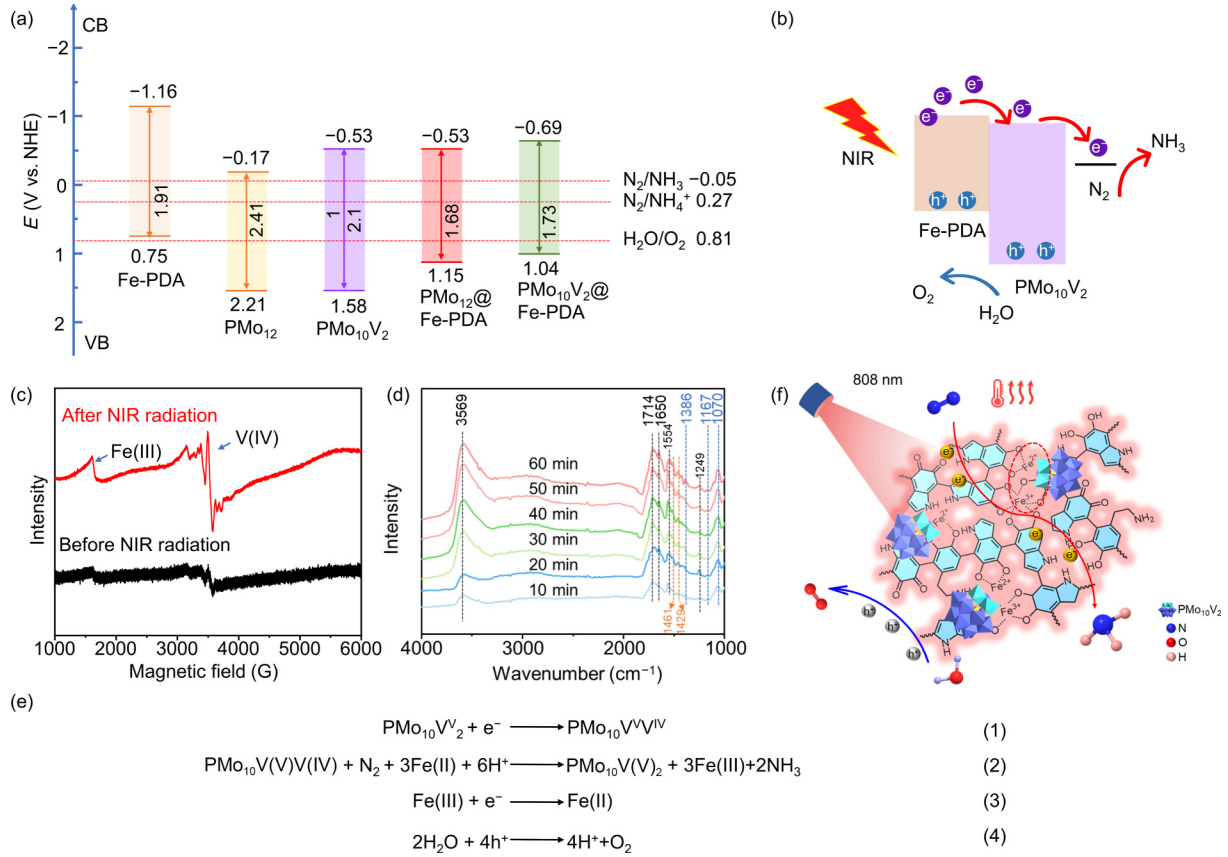

Figure 4 (a) Energy diagram of Fe-PDA, PMo_{12}, $PMo_{10}V_2$, PMo_{12}@Fe-PDA and $PMo_{10}V_2$@Fe-PDA. (b) Electron transfer pathway of N_2 reduction over $PMo_{10}V_2$@Fe-PDA under NIR laser light radiation. (c) The EPR spectra of $PMo_{10}V_2$@Fe-PDA before and after NIR laser light radiation. (d) *In-situ* DRIFTS spectra were taken during photothermal catalytic N_2 fixation in the presence of water vapor over $PMo_{10}V_2$@Fe-PDA. (e) The proposed reaction mechanism of N_2 reduction over $PMo_{10}V_2$@Fe-PDA under NIR radiation. (f) Schematic diagram of NIR photothermal catalysis for N_2 reduction over $PMo_{10}V_2$@Fe-PDA catalysts.

1714 and 1650 cm^{-1} were ascribed to the N–H stretching mode and bending mode. The peaks at 1070, 1167 and 1386 cm^{-1} were assigned to N–N stretching vibration of the NH_2–NH_2, NH–NH_2, NH–NH, and the peaks at 1249 cm^{-1} were caused by vibration modes of N–N of the NH_2–NH_2. The bands at 1429 and 1461 cm^{-1} are N–H symmetric vibrations of adsorption NH_4^+. While the bands at 1554 cm^{-1} were attributed to the absorption of NH_3 molecules [41–43]. The evidence provides powerful proof that N_2 could be continuously weakened by the NIR light until N_2 molecule cleavages to NH_3 or NH_4^+ in the final step. So, the detailed mechanism is listed as follows (Fig. 4(e)). Under NIR light radiation, the photothermal effect of Fe-PDA promotes to formation of high-energy electrons. According to EPR results and electronic band structure distribution diagram, the generated hot electrons should tend to migrate from Fe-PDA to the $PMo_{10}V(V)V(V)$, thus generating the reduced $PMo_{10}V(V)V(IV)$ that has strong reducibility (Eq. (1)). Meanwhile, the reduced $PMo_{10}V(V)V(IV)$ and Fe (II) expose many empty 3d orbitals to enhance the N_2 adsorption amount and the strong coordination between Fe(II), V(IV) and N_2, which will weaken the nonpolar N_2 molecule and reacts with the free H^+ to form NH_3, accompanying by V(IV) return to the initial state V(V) and Fe(II) oxidize to Fe(III) (Eq. (2)). Moreover, the electrons are used to reduce Fe(III) to Fe(II) (Eq. (3)). At this point, H_2O is oxidated by the hole to form O_2 (Eq. (4)). Totally, the formed V(V)/V(IV) and Fe(III)/Fe(II) not only adsorbes and activates N_2 molecules but also promotes the electron transfer between $PMo_{10}V_2$@Fe-PDA and N_2; On the other hand, Fe(III) in Fe-PDA serve as *in situ* photothermal conversion heater centers. Upon NIR laser radiation, the Fe(III)-PDA could generate a local high temperature, which further effectively activates the N≡N triple bond adsorbed near the catalysts and accelerates the mass transfer of N_2 adsorbed on the catalysts, thereby synergistically reinforcing the N_2 reduction reactions (Fig. 4(f)).

4 Conclusions

By anchoring with or without V-substituted POMs onto the photothermal carrier Fe-PDA through electrostatic interaction, two NIR photothermal catalysts based on "FeV" cofactors are fabricated for photothermal catalysis N_2 reduction. Fe-PDA, as the cation supports, not only allows POMs to spread evenly, but also supports the adsorption of N_2. Fe-PDA as a linker greatly shortens the distance between ions Fe and V. Under NIR illumination, the prepared $PMo_{10}V_2$@Fe-PDA enhances electron transfer between V(V)/V(IV) and Fe(III)/Fe(II) and N_2 molecules adsorbed, reducing the carrier recombination. More importantly, after iron chelated PDA, the photothermal effect is enhanced, it acts as a local heater close to the FeV catalytic site. The local heating from the supports becomes a unique source for accelerating the catalytic reaction. With the designed catalysts possessing integrated multi-functions, $PMo_{10}V_2$@Fe-PDA exhibits prominent NH_3 production performance in pure water without any other sacrificial agent and cocatalyst under 808 nm NIR laser light at atmospheric pressure. It reaches 181.1 $\mu mol \cdot L^{-1}$ NH_3 with a turnover frequency of 1006.1 $mmol \cdot M^{-1} \cdot h^{-1}$, which is higher than the previously reported photocatalysts. The mild conditions, high production for N_2 reduction and constitute an applicable strategy of catalysts in green chemistry. We expect that such a NIR photothermal catalysis system could provide an alternative approach to preparing green catalysts for energy chemistry.

Electronic Supplementary Material: Supplementary material (preparation of Fe-PDA, basic characterization of POMs@Fe-PDA, FT-IR, DLS, ICP, XPS, UPS, EDX energy spectra, photothermal conversion efficiency, photothermal catalysis of N_2 reduction, and characterization of recycled POMs@Fe-PDA) is available in the online version of this article at https://doi.org/10.26599/NR.2025.94907006.

Data availability

All data needed to support the conclusions in the paper are presented in the manuscript and the Electronic Supplementary Material. Additional data related to this paper may be requested from the corresponding author upon request.

Acknowledgements

This work was financially supported by the National Natural Science Foundation of China (No. 22302055), the Key Scientific Research Project Plan of Colleges and Universities of Henan Province (No. 24B150004), and the Natural Science Foundation of Henan Province, China (No. 232300421369).

Declaration of competing interest

All the contributing authors report no conflict of interests in this work.

Author contribution statement

X. F. C.: Data curation, project administration, validation, writing manuscript, experimental design. L. X. W. and F. B.: Project administration, finished the final version of the manuscript. All the authors have approved the final manuscript.

Use of AI statement

None.

References

[1] Tanabe, Y.; Nishibayashi, Y. Comprehensive insights into synthetic nitrogen fixation assisted by molecular catalysts under ambient or mild conditions. *Chem. Soc. Rev.* **2021**, *50*, 5201–5242.

[2] Zehr, J. P.; Capone, D. G. Changing perspectives in marine nitrogen fixation. *Science* **2020**, *368*, eaay9514.

[3] Cheng, M.; Xiao, C.; Xie, Y. Shedding light on the role of chemical bond in catalysis of nitrogen fixation. *Adv. Mater.* **2021**, *33*, 2007891.

[4] Liu, Y. L.; Zhuang, Z. C.; Liu, Y. X.; Liu, N. Y.; Li, Y. X.; Cheng, Y. Y.; Yu, J. W.; Yu, R. H.; Li, H. T.; Wang, D. S. Shear-strained Pd single-atom electrocatalysts for nitrate reduction to ammonia. *Angew. Chem., Int. Ed.* **2024**, e202411396.

[5] Luo, Y. R.; Chen, G. F.; Ding, L.; Chen, X. Z.; Ding, L. X.; Wang, H. H. Efficient electrocatalytic N_2 fixation with MXene under ambient conditions. *Joule* **2019**, *3*, 279–289.

[6] Peng, Y.; Albero, J.; Franconetti, A.; Concepción, P.; García, H. Visible and NIR light assistance of the N_2 reduction to NH_3 catalyzed by Cs-promoted Ru nanoparticles supported on strontium titanate. *ACS Catal.* **2022**, *12*, 4938–4946.

[7] Hui, X. C.; Li, L. F.; Xia, Q. N.; Hong, S.; Hao, L. D.; Robertson, A. W.; Sun, Z. Y. Interface engineered $Sb_2O_3/W_{18}O_{49}$ heterostructure for enhanced visible-light-driven photocatalytic N_2 reduction. *Chem. Eng. J.* **2022**, *438*, 135485.

[8] Dong, G. J.; Huang, X. J.; Bi, Y. P. Anchoring black phosphorus quantum dots on Fe-doped $W_{18}O_{49}$ nanowires for efficient photocatalytic nitrogen fixation. *Angew. Chem., Int. Ed.* **2022**, *61*, e202204271.

[9] Yuan, Y. J.; Wang, P.; Li, Z. J.; Wu, Y. Z.; Bai, W. F.; Su, Y. B.; Guan, J.; Wu, S. T.; Zhong, J. S.; Yu, Z. T. et al. The role of bandgap and interface in enhancing photocatalytic H_2 generation activity of 2D-2D black phosphorus/MoS_2 photocatalyst. *Appl. Catal. B: Environ.* **2019**, *242*, 1–8.

[10] Wang, G. X.; Li, B. J.; Li, B.; Wu, L. X. Gold nanocrystal-loaded 2D supramolecular network for plasmon-enhanced nitrogen fixation. *Green Chem.* **2023**, *25*, 10556–10566.

[11] Li, X. H.; Li, H.; Jiang, S. L.; Yang, L.; Li, H. Y.; Liu, Q. L.; Bai, W.; Zhang, Q.; Xiao, C.; Xie, Y. Constructing mimic-enzyme catalyst: Polyoxometalates regulating carrier dynamics of metal-organic frameworks to promote photocatalytic nitrogen fixation. *ACS Catal.* **2023**, *13*, 7189–7198.

[12] Han, Q. T.; Bai, X. W.; Chen, J. M.; Feng, S. N.; Gao, W.; Tu, W. G.; Wang, X. Y.; Wang, J. L.; Jia, B.; Shen, Q. et al. Hollow $InVO_4$ nanocuboid assemblies toward promoting photocatalytic N_2 conversion performance. *Adv. Mater.* **2021**, *33*, 2006780.

[13] Zhao, Y. F.; Gao, W.; Li, S. W.; Williams, G. R.; Mahadi, A. H.; Ma, D. Solar- versus thermal-driven catalysis for energy conversion. *Joule* **2019**, *3*, 920–937.

[14] Mateo, D.; Cerrillo, J. L.; Durini, S.; Gascon, J. Fundamentals and applications of photo-thermal catalysis. *Chem. Soc. Rev.* **2021**, *50*, 2173–2210.

[15] Chen, X. F.; Zhang, G. H.; Li, B.; Wu, L. X. An integrated giant polyoxometalate complex for photothermally enhanced catalytic oxidation. *Sci. Adv.* **2021**, *7*, eabf8413.

[16] Chen, X. F.; Wei, M. F.; Yang, A. B.; Jiang, F. R.; Li, B.; Kholdeeva, O. A.; Wu, L. X. Near-infrared photothermal catalysis for enhanced conversion of carbon dioxide under mild conditions. *ACS Appl. Mater. Interfaces* **2022**, *14*, 5194–5202.

[17] Zhao, Z. F.; Yang, D.; Ren, H. J.; An, K.; Chen, Y.; Zhou, Z. Y.; Wang, W. J.; Jiang, Z. Y. Nitrogenase-inspired mixed-valence MIL-53(Fe^{II}/Fe^{III}) for photocatalytic nitrogen fixation. *Chem. Eng. J.* **2020**, *400*, 125929.

[18] Spatzal, T.; Schlesier, J.; Burger, E. M.; Sippel, D.; Zhang, L. M.; Andrade, S. L. A.; Rees, D. C.; Einsle, O. Nitrogenase FeMoco investigated by spatially resolved anomalous dispersion refinement. *Nat. Commun.* **2016**, *7*, 10902.

[19] Meredith, P.; Sarna, T. The physical and chemical properties of eumelanin. *Pigm. Cell Res.* **2006**, *19*, 572–594.

[20] Lv, J. Y.; Xing, Y.; Li, X. Y.; Du, X. NIR light-propelled bullet-shaped carbon hollow nanomotors with controllable shell thickness for the enhanced dye removal. *Exploration* **2022**, *2*, 20210162.

[21] Xu, N.; Hu, A.; Pu, X. M.; Li, J. F.; Wang, X. M.; Wang, J.; Huang, Z. B.; Liao, X. M.; Yin, G. F. Fe(III)-chelated polydopamine nanoparticles for synergistic tumor therapies of enhanced photothermal ablation and antitumor immune activation. *ACS Appl. Mater. Interfaces* **2022**, *14*, 15894–15910.

[22] Zhu, Y. D.; Xin, N. N.; Qiao, Z.; Chen, S. P.; Zeng, L. W.; Zhang, Y. S.; Wei, D.; Sun, J.; Fan, H. S. Novel tumor-microenvironment-based sequentialcatalytic therapy by Fe(II)-engineered polydopamine nanoparticles. *ACS Appl. Mater. Interfaces* **2019**, *11*, 43018–43030.

[23] Zhang, G. H.; Li, X. Y.; Chen, G.; Zhang, Y.; Wei, M. F.; Chen, X. F.; Li, B.; Wu, Y. Q.; Wu, L. X. Supramolecular framework membrane for precise sieving of small molecules, nanoparticles and proteins. *Nat. Commun.* **2023**, *14*, 975.

[24] Guan, W. M.; Wang, G. X.; Li, B.; Wu, L. X. Organic macrocycle-polyoxometalate hybrids. *Coord. Chem. Rev.* **2023**, *481*, 215039.

[25] Yamaguchi, M.; Shioya, K.; Li, C. F.; Yonesato, K.; Murata, K.; Ishii, K.; Yamaguchi, K.; Suzuki, K. Porphyrin-polyoxotungstate molecular hybrid as a highly efficient, durable, visible-light-responsive photocatalyst for aerobic oxidation reactions. *J. Am. Chem. Soc.* **2024**, *146*, 4549–4556.

[26] Pope, M. T.; Müller, A. Polyoxometalate chemistry: An old field with new dimensions in several disciplines. *Angew. Chem., Int. Ed.* **1991**, *30*, 34–48.

[27] Chen, X. F.; Yang, A. B.; Wang, G. X.; Wei, M. F.; Liu, N.; Li, B.; Wu, L. X. Reinforced catalytic oxidation of polyoxometalate@charge transfer complex by on-site heating from photothermal conversion. *Chem. Eng. J.* **2022**, *446*, 137134.

[28] Huang, Q.; Liu, J.; Feng, L.; Wang, Q.; Guan, W.; Dong, L. Z.; Zhang, L.; Yan, L. K.; Lan, Y. Q.; Zhou, H. C. Multielectron transportation of polyoxometalate-grafted metalloporphyrin coordination frameworks for selective CO_2-to-CH_4 photoconversion. *Natl. Sci. Rev.* **2020**, *7*, 53–63.

[29] Li, X. H.; Chen, W. L.; Tan, H. Q.; Li, F. R.; Li, J. P.; Li, Y. G.; Wang, E. B. Reduced state of the graphene oxide@polyoxometalate nanocatalyst achieving high-efficiency nitrogen fixation under light driving conditions. *ACS Appl. Mater. Interfaces* **2019**, *11*, 37927–37938.

[30] Tsigdinos, G. A.; Hallada, C. J. Molybdovanadophosphoric acids and their salts. I. Investigation of methods of preparation and characterization. *Inorg. Chem.* **1968**, *7*, 437–441.

[31] Kumar, A.; Kumar, S.; Kumari, N.; Lee, S. H.; Han, J.; Michael, I. J.; Cho, Y. K.; Lee, I. S. Plasmonically coupled nanoreactors for NIR-light-mediated remote stimulation of catalysis in living cells. *ACS Catal.* **2019**, *9*, 977–990.

[32] Qiu, J. C.; Shi, Y. F.; Xia, Y. N. Polydopamine nanobottles with photothermal capability for controlled release and related applications. *Adv. Mater.* **2021**, *33*, 2104729.

[33] Wu, Y. Z.; Zhou, W. Q.; Zhou, L.; In, S. I.; Lei, J. Y.; Wang, L. Z.; Zhang, J. L.; Liu, Y. D. Near-infrared photothermal effect enhanced heterogeneous catalysis of Co_3O_4/PDA composite for highly efficient activation of peroxymonosulfate to degrade antibiotic pollutants. *Chem. Eng. J.* **2023**, *474*, 145267.

[34] Andersen, S. Z.; Čolić, V.; Yang, S.; Schwalbe, J. A.; Nielander, A. C.; McEnaney, J. M.; Enemark-Rasmussen, K.; Baker, J. G.; Singh, A. R.; Rohr, B. A. et al. A rigorous electrochemical ammonia synthesis protocol with quantitative isotope measurements. *Nature* **2019**, *570*, 504–508.

[35] Suryanto, B. H. R.; Du, H. L.; Wang, D. B.; Chen, J.; Simonov, A. N.; MacFarlane, D. R. Challenges and prospects in the catalysis of electroreduction of nitrogen to ammonia. *Nat. Catal.* **2019**, *2*, 290–296.

[36] Huang, H. J.; Yu, D. S.; Hu, F.; Huang, S. C.; Song, J. N.; Chen, H. Y.; Li, L. L.; Peng, S. J. Clusters induced electron redistribution to tune oxygen reduction activity of transition metal single-atom for metal-air batteries. *Angew. Chem., Int. Ed.* **2022**, *61*, e202116068.

[37] Zhao, Y. X.; Shi, R.; Bian, X. A. N.; Zhou, C.; Zhao, Y. F.; Zhang, S.; Wu, F.; Waterhouse, G. I. N.; Wu, L. Z.; Tung, C. H. et al. Ammonia detection methods in photocatalytic and electrocatalytic experiments: How to improve the reliability of NH_3 production rates. *Adv. Sci.* **2019**, *6*, 1802109.

[38] Comer, B. M.; Liu, Y. H.; Dixit, M. B.; Hatzell, K. B.; Ye, Y. F.; Crumlin, E. J.; Hatzell, M. C.; Medford, A. J. The role of adventitious carbon in photo-catalytic nitrogen fixation by titania. *J. Am. Chem. Soc.* **2018**, *140*, 15157–15160.

[39] Zhang, X. R.; Shi, R.; Li, Z. H.; Zhao, J. Q.; Huang, H. N.; Zhou, C.; Zhang, T. R. Photothermal-assisted photocatalytic nitrogen oxidation to nitric acid on palladium-decorated titanium oxide. *Adv. Energy Mater.* **2022**, *12*, 2103740.

[40] Nambu, J. C.; Ueda, T.; Guo, S. X.; Boas, J. F.; Bond, A. M. Detailed voltammetric and EPR study of protonation reactions accompanying the one-electron reduction of Keggin-type polyoxometalates, $[XV^{V}M_{11}O_{40}]^{4-}$ (X = P, As; M = Mo, W) in acetonitrile. *Dalton Trans.* **2010**, *39*, 7364–7373.

[41] Bo, Y. N.; Wang, H. Y.; Lin, Y. X.; Yang, T.; Ye, R.; Li, Y.; Hu, C. Y.; Du, P. Y.; Hu, Y. G.; Liu, Z. et al. Altering hydrogenation pathways in photocatalytic nitrogen fixation by tuning local electronic structure of oxygen vacancy with dopant. *Angew. Chem., Int. Ed.* **2021**, *60*, 16085–16092.

[42] Yuan, J.; Feng, W. H.; Zhang, Y. F.; Xiao, J. Y.; Zhang, X. Y.; Wu, Y. T.; Ni, W. K.; Huang, H. W.; Dai, W. X. Unraveling synergistic effect of defects and piezoelectric field in breakthrough piezo-photocatalytic N_2 reduction. *Adv. Mater.* **2024**, *36*, 2303845.

[43] Mao, C. L.; Wang, J. X.; Zou, Y. J.; Shi, Y. B.; Viasus, C. J.; Loh, J. Y. Y.; Xia, M. K.; Ji, S. F.; Li, M. Q.; Shang, H. et al. Photochemical acceleration of ammonia production by Pt_1–Pt_n–TiN reduction and N_2 activation. *J. Am. Chem. Soc.* **2023**, *145*, 13134–13146.